Chapter 5

Energy Transfer Dynamics, Emission Color Tuning, and Fluorescence Thermometry in Dy^{3+}/Eu^{3+} co-doped $SrMoO_4$ phosphors

Herein, we discuss the energy transfer dynamics, emission color tuning, and fluorescence thermometry in Dy^{3+}/Eu^{3+} co-doped $SrMoO_4$ phosphors. Our work demonstrates a viable scheme for tailoring the PL emission of single-phase phosphors through precisely controlling dopant concentrations and by modulating excitation wavelength. The overall emission is tuned from greenish-yellow to white and greenish-yellow to reddish-orange. A detailed energy transfer process from the host to the Ln^{3+} ions and between the Ln^{3+} ions is discussed. The fluorescence thermometry is studied by examining the fluorescence intensity ratio of Dy^{3+} and Eu^{3+} PL intensities monitored at 297 nm. This research opens up new avenues for the development of color-tunable luminous materials for various optoelectronic and temperature sensing applications.

5.1 Introduction

In chapters 3 and 4 we discussed the utility of $SrMoO_4$ phosphor as a host for synthesizing Sm^{3+} doped red-emitting phosphors and also studied the effect of dopants such as Bi^{3+} and Zn^{2+} in improving the crystallinity and thereby enhancing the red emission of $SrMoO_4:Sm^{3+}$ phosphor. In this chapter, we focus on two other important applications of the $SrMoO_4$ phosphor which are color tunability and fluorescence thermometry.

Scientists have endeavored in the exploration and modification of new phosphors for the acquisition of tunable color emission owing to their demand in a variety of applications such as multicolor display devices, encrypted information storage, white light-emitting diode (wLED), biological applications, fluorescent sensors and so on [159–162]. In general, color tunability is achieved by modifications in the crystal structure, doping multiple rare-earth (RE) ions, altering the excitation wavelength, crystal site engineering, or changing the temperature [163–165]. Recently, much attention has been paid to developing single ingredient phosphor for the production of tunable light sources for different applications such as field emission displays, multicolor three-dimensional displays, full-color flat panel displays, and so on [166,167]. The single-phase phosphors with tunable emission possess certain advantages specifically suitable correlated color temperature (CCT) and adjustable color rendering index (CRI) values, which are desirable for developing tunable light sources. Moreover, these phosphors would make device packaging easier.

The intriguing 4f-4f, 5d-4f, and charge transfer (CT) transitions (ligand to metal or metal to ligand) of RE ions have made these ions key components in various emerging applications such as fluorescence thermometry, lighting devices, optical fibres, solar cells, display devices, lasers, and optical probes in biological applications [13,37–41,168]. The 5d-4f and 4f-4f transitions of the different lanthanide ions result in broad emission bands and

sharp spectral lines, respectively, which range from UV to infrared region, and these transitions are influenced by the polarizability and the ligand field of the parent crystal. Over the past few years, the RE-doped phosphors have sparked a lot of interest in developing spectrally adjustable phosphors via co-activation. Among the different lanthanide ions, the Dy^{3+} ion with its yellow ($^4F_{9/2} \rightarrow {}^6H_{13/2}$) and blue ($^4F_{9/2} \rightarrow {}^6H_{15/2}$) emissions has been utilized for the emission of neutral white light[169,170]. However, such white light is devoid of a red component which results in low CRI and elevated CCT value. Nevertheless, doping of red-emitting RE ions such as Eu^{3+} can shift the overall white light emission of the phosphor towards the red region. Therefore, cool to warm white light color tunability could be accomplished by precisely controlling the doping concentration of Dy^{3+} and Eu^{3+} ions in the host and also by altering the excitation energy.

One of the essential considerations for RE-based phosphors is the host lattice. Different host lattice such as vanadates [34], sulfides [171], phosphates [172], silicates [8], garnets [173], molybdates [174], nitrides [56], or oxinitrides [175] has been explored as host lattice for RE ions for specific applications. Among all these, the molybdate-based RE compounds have drawn attention to serving as luminescent hosts owing to their excellent properties and easy synthesis. The molybdate compounds have near-ultraviolet (UV) excitation, blue-green broadband emission, high solubility of RE ions, and good chemical and thermal stability [176,177]. In this work, we have chosen $SrMoO_4$ as our model host lattice. Particularly, the $SrMoO_4$ phosphor is known as a self-activated luminous phosphor that shows a CT absorption band of $[MoO_4]^{2-}$ groups owing to charge transfer from O^{2-} to Mo^{6+}, situated near the UV region and has greenish-blue emission [23,24]. The $SrMoO_4$ phosphor shows the successful transfer of the energy from the Mo^{6+} to the excited energy levels of the RE ions

and this property can be utilized for exhibiting spectral color tunability in RE-doped $SrMoO_4$ phosphor.

Apart from tunable color light sources, phosphor materials have also been studied to develop a fluorescent-based thermometer. Fluorescence thermometry alleviates the problems inherent with traditional temperature sensor systems as it provides a non-invasive mode of operation, electromagnetic passivity, fast response, remote readouts, and high-temperature sensitivity. Various temperature-dependent spectral parameters such as spectral position, polarization, fluorescence intensity ratio (FIR), fluorescence lifetime, and bandwidth can be adopted to determine temperature [67,72,178]. Among these, FIR is one of the most reliable thermometric parameters for fluorescence thermometry because of its relatively high resistance to environmental interference. Many RE has thermally coupled energy levels (TCELs) such as Eu^{3+} ($^5D_0$ and $^5D_1$) [79], Dy^{3+} ($^4I_{15/2}$ and $^4F_{9/2}$) [14], Er^{3+} ($^2H_{11/2}$ and $^4S_{3/2}$) [5], and Nd^{3+} ($^4F_{5/2}$ and $^4F_{3/2}$) [80] which is utilized for FIR based fluorescence thermometry. Among these RE ions, the Eu^{3+} and Dy^{3+} ions exhibit red, blue, and yellow emissions as a result of the $^5D_0 \rightarrow {}^7F_2$ (Eu^{3+}), $^4F_{9/2} \rightarrow {}^6H_{15/2}$ (Dy^{3+}), and $^4F_{9/2} \rightarrow {}^6H_{13/2}$ (Dy^{3+}) transitions under UV excitation. In this work, we have used a mixed lanthanide (Dy^{3+}, Eu^{3+}) approach, which is based on the simultaneous emission of two Ln^{3+} ions from the same host material to design fluorescence ratiometric thermometers. The combination of Dy^{3+}/Eu^{3+} is preferred over the other Ln^{3+} combinations as the emission lines of Dy^{3+} and Eu^{3+} are well separated and thus provide better color discriminability with increase in temperature. Moreover, Eu^{3+} is preferred over other red emitting ions such as Sm^{3+} because Eu^{3+} ion has higher emission intensity compared to the Sm^{3+} ion in molybdate host which makes it more suitable for the optical thermometry application. However, a small overlap between Dy^{3+} excitation spectra and Eu^{3+} emission spectra impose difficulty in realizing the

effective transfer of energy from Dy^{3+} to Eu^{3+} ions, therefore, it is crucial to find an appropriate host phosphor having a wide absorption band and the ability to sensitize Dy^{3+} and Eu^{3+} ions simultaneously. To overcome this limitation we have chosen $SrMoO_4$ as a host phosphor for Dy^{3+} and Eu^{3+} ions and observed an efficient transfer of energy from the excited band of the host to the excited energy levels of Dy^{3+} and Eu^{3+} ions. We have observed that the rise in temperature leads to the anti-thermal quenching in Dy^{3+} emission and thermal quenching in Eu^{3+} emission, causing contrasting variations in the emission peak intensity of the two RE ions. We have exploited this contrasting nature of Dy^{3+} and Eu^{3+} emission with rising temperature to investigate the FIR-based temperature sensing.

In this chapter, we have adopted a urea-based auto-combustion process for the synthesis. The auto-combustion process is an attractive alternative to the conventional synthesis methods as it offers various advantages such as simplicity, narrow particle size distribution, and cost-efficiency [141,179]. We have studied the luminescent properties and decay dynamics thoroughly and explored the involved transfer of energy from host to dopant ions and from Dy^{3+} to Eu^{3+} ions. We have also accomplished spectral tunability by adjusting the concentration of RE ions in $SrMoO_4$ and by altering the excitation energy. The phosphors were also studied for the fluorescence thermometry application. Thus, our studied phosphors can potentially be used in crucial applications such as w-LEDs, spectrally tunable devices, and fluorescence thermometers.

5.2 Experimental

5.2.1 Chemicals

The raw materials for the synthesis were strontium oxide, dysprosium nitrate, europium nitrate, and ammonium molybdate (para) tetrahydrate. All precursors were purchased from Sigma-Aldrich. The Dy^{3+} (0%, 2%, 3%, 4%, 5%) doped $SrMoO_4$ and Eu^{3+} (1%, 2%, 3%,

and 4%) co-doped in 4% Dy^{3+} doped $SrMoO_4$ phosphor are classified as D0, D2, D3, D4, D5, E1, E2, E3, and E4, respectively.

5.2.2 Synthesis Process

A simple urea-assisted auto combustion procedure was used to synthesize the phosphors. The stoichiometric quantity of strontium oxide and RE nitrates were taken in a clean beaker then HNO_3 was gradually poured over it. After adding around 10 mL of nitric acid, the solution was constantly stirred for 1 hour. To eliminate the surplus acid, the mixture was placed under constant heating and enriched with double-distilled (DD) water. The stoichiometric quantity of molybdate precursor was mixed with DD water in another beaker and placed with constant stirring for 2 hours. The Urea was mixed with the molybdate solution. Metal nitrates and urea had a mole ratio of 2:1. After that both the solutions were mixed and then the resulting solution was maintained at 100 °C until the surplus water was evaporated. After drying, the mixture was placed in a hot air oven preset to 250 °C for 12 hours. The material was then powdered and put in a closed furnace for 4 hours of calcination at 1000 °C. The same process was used to synthesize all of the phosphors.

5.2.3 Characterisation

The XRD data was recorded using Cu K_α radiation ($\lambda = 1.54$ Å) in the powder x-ray diffractometer (Rigaku-Mini FlexII). The structural refinement was done with the help of FULLPROF software [119]. The spectrometer (JASCO FT/IR 4600 having an attenuated total reflection setup with a diamond disc as an internal reflection element) was used to record the FTIR scans of the phosphors. The absorption analysis was done using the UV-Vis-NIR spectrophotometer (JASCO V770) fitted with an integrating sphere setup. The absorption spectra of the powdered samples were obtained in an absorption mode after the baseline correction using barium sulfate as a reference. The Photoluminescence excitation (PLE),

emission (PL), and temperature-dependent PL (TDPL) spectra analysis were done using a spectrophotometer (Horiba Fluorolog-3). The slit width of the PL spectrophotometer was fixed at 1 nm for all the measurements. The PL lifetime was measured with a FLS920 Fluorescence spectrometer (Edinburgh Instruments) fitted with a 60 W xenon flash lamp. The X-ray photoelectron spectrometer (Thermo Fischer Scientific ESCALAB Xi) was utilized for XPS measurements.

5.3 Results and Discussion

5.3.1 Structural and compositional properties

The Rietveld refinement of the XRD pattern is performed to identify the crystal structure of the prepared samples. Fig. 5.1 (a) illustrates the Rietveld refined XRD patterns of D0, D4, and E4 phosphors scanned over the $20^o \leq 2\theta \leq 80^o$ range.

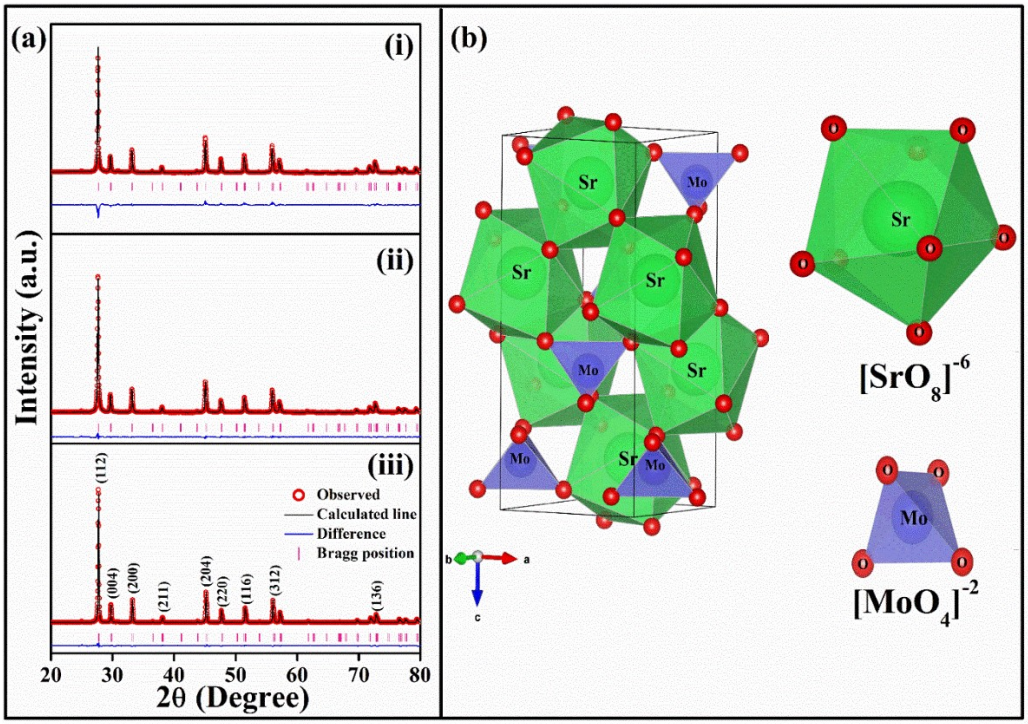

Fig. 5.1 (a) XRD patterns of **(i)** E4, **(ii)** D4, and **(iii)** D0 phosphors along with their Rietveld refinement profile. **(b)** $SrMoO_4$ crystal structure with SrO_8 dodecahedron and MoO_4 tetrahedron.

The tetragonal crystal structure with the $I4_1/a$ space group of all the phosphors is confirmed. Some prominent peaks are labeled in the XRD graph and found in accord with the previous results [20,23,45,143]. The Dy^{3+} (1.02 Å) and Eu^{3+} (1.06 Å) ions are likely to replace Sr^{2+} (1.26 Å) ions because all three have a comparable ionic radius for the system with coordination number = 8 [144]. Fig. 5.1 (b) depicts the tetragonal crystal structure of $SrMoO_4$. The Sr^{2+} ions are forming SrO_8 dodecahedral with eight oxygen ions, whereas, Mo^{6+} ions are forming MoO_4 tetrahedron which is coordinated by four oxygen ions [24]. The lattice parameters, atomic positions, and volume of the unit cell of D0, D4, and E4 phosphors are summarized in Table 5.1.

Table 5.1 Atomic positions, unit cell volume, and lattice parameters of D0, D4, and E4 phosphors.

Parameters	**D0**	**D4**	**E4**
Atomic positions (x,y,z):			
Eu/Dy/Sr	(0,0.250,0.625)	(0,0.250,0.625)	(0,0.250,0.625)
Mo	(0,0.250,0.125)	(0,0.250,0.125)	(0,0.250,0.125)
O	(0.2384,0.1132,0.0449)	(0.2396,0.1128,0.0444)	(0.2383,0.1096,0.0442)
Angles (α, β, γ) in degree	(90, 90, 90)	(90, 90, 90)	(90, 90, 90)
Lattice parameters (Å)			
a	5.398	5.392	5.384
c	12.033	12.016	12.000
Unit cell volume ($Å^3$)	350.658	349.377	347.530
Bond lengths (Å)			
Sr/DyEu/-O1	2.597 (3)	2.595 (3)	2.569 (3)
Sr/Dy/Eu-O2	2.588 (3)	2.581 (3)	2.616 (3)
Mo-O	1.766 (3)	1.775 (3)	1.752 (5)
$R_{Factors}$			
R_p	5.98	8.76	18.4
R_{wp}	6.90	9.24	16.5
χ^2	4.09	3.98	8.25

The decrement in value of lattice parameters and consequent contraction of unit cell volume results from the variation between the ionic radius of the lanthanide dopants (Dy^{3+} and Eu^{3+}) and Sr^{2+} ion [23,24].

The FTIR technique is employed to investigate the IR active modes present in the phosphors. The FTIR spectra of D0, D4, and E3 phosphors in the transmittance mode are shown in Fig. 5.2 The antisymmetric stretched vibrations corresponding to O—Mo stretching in $SrMoO_4$ are represented by the vibrational band from 545 cm^{-1} to 908 cm^{-1} [145,146]. The vibrational band near 400 cm^{-1} reflects the O—Mo—O bending vibrational mode present in the $SrMoO_4$ [145,146]. The band from 2315 cm^{-1} to 2375 cm^{-1} is because of the presence of the C—O asymmetric stretching [141]. No significant shift in the vibration bands is detected as a result of doping. The FTIR spectra further justify the development of the crystalline phase of D0, D4, and E3 samples.

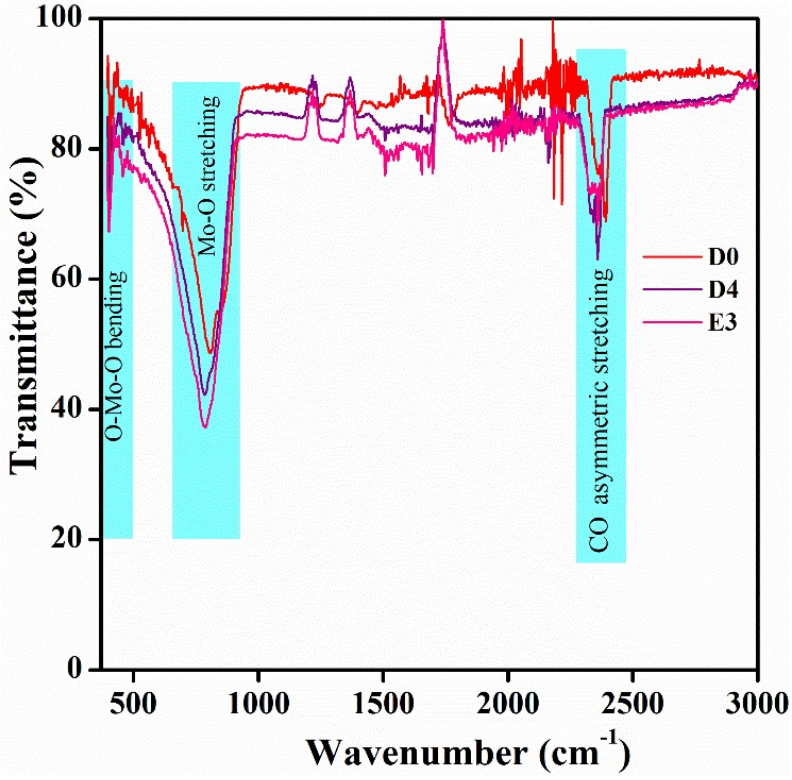

Fig. 5.2 FTIR spectra of D0, D4, and E3 phosphor

The confirmation of the oxidation state of the elements that existed on the surface of the D4 and E4 phosphors is done using the XPS investigation. The C 1s line at 284.6 eV, which arises owing to the existence of unintended carbon on the surface of the phosphors during ambient exposure, is used for charge correction of XPS spectra of all the elements. Survey scans of both the phosphors, shown in Fig. 5.3 (a), validate the existence of the major peaks related to Mo, Sr, Dy, Eu, and O. All the peaks in the survey scan are verified by the national institute of a standard technology XPS database [147]. The survey scans also confirm that there are no other impurities in the sample than carbon. Fig. 5.3 (b) to (f) show the XPS binding energy (BE) plots of the 3d states of Sr, Mo, Dy, and Eu 3d and 1s state of O for the D4 and E4 phosphors, and Table 5.2 lists the corresponding B.E.). The strontium BE spectrum as presented in Fig. 5.3 (b), is composed of two main peaks corresponding to $3d_{3/2}$ and $3d_{5/2}$ positioned at 134.0 eV and 132.4 eV, respectively [129]. The strontium XPS graph verifies the divalent oxidation state of strontium. Fig. 5.3 (c) presents the Mo 3d core-level spectra with peaks at ~234.8 eV and ~231.6 eV that are accredited to $3d_{3/2}$ and $3d_{5/2}$ levels of Mo^{6+}, respectively. The Mo 3d XPS spectra confirm the +6 oxidation state of Mo [112,129]. Fig. 5.3 (d) depicts the O 1s peak at ~529.5 eV. Fig. 5.3 (e) presents the XPS spectra of Dy 3d for both the phosphors. The two strong peaks at ~1334.4 eV and ~1303.2 eV represent the $3d_{3/2}$ and $3d_{5/2}$ core level spin-orbit splitting components of Dy, respectively [112]. The XPS spectra substantiate that the dysprosium ions are in the trivalent oxidation state. The XPS spectra in Fig. 5.3 (f) depict the Eu 3d core-level spectra for E4 phosphor. The spectra contain four peaks ascribed to Eu^{2+} and Eu^{3+} levels. The peaks at 1163.8 eV and 1133.5 eV are accredited to $3d_{3/2}$ and $3d_{5/2}$ levels of Eu^{3+}. The peak to peak value for these two peaks is 29.9 eV, which again validates the trivalent oxidation state of Eu 3d [180]. Two additional peaks at 1153.4 eV and 1133.5 eV are accredited to the $3d_{3/2}$ and $3d_{5/2}$ levels of Eu^{2+}. The

Eu 3d XPS spectrum validates the existence of Eu ions in the +2 and +3 oxidation states in E4 phosphor [141].

Table 5.2 The B.E of the elements present in D4 and E4 samples based on their XPS spectra.

Elements	Oxidation State	Binding energy (eV)	
		D4	E4
Sr	Sr^{2+} $3d_{3/2}$	134.0	134.0
	Sr^{2+} $3d_{5/2}$	132.4	132.3
Mo	Mo^{6+} $3d_{3/2}$	234.8	234.7
	Mo^{6+} $3d_{5/2}$	231.6	231.6
O	O 1s	529.5	529.5
Dy	Dy^{3+} $3d_{3/2}$	1334.4	1334.1
	Dy^{3+} $3d_{5/2}$	1303.2	1304.1
Eu	Eu^{3+} $3d_{3/2}$	-	1163.8
	Eu^{3+} $3d_{5/2}$	-	1133.4
	Eu^{2+} $3d_{3/2}$	-	1153.4
	Eu^{2+} $3d_{5/2}$	-	1124.0

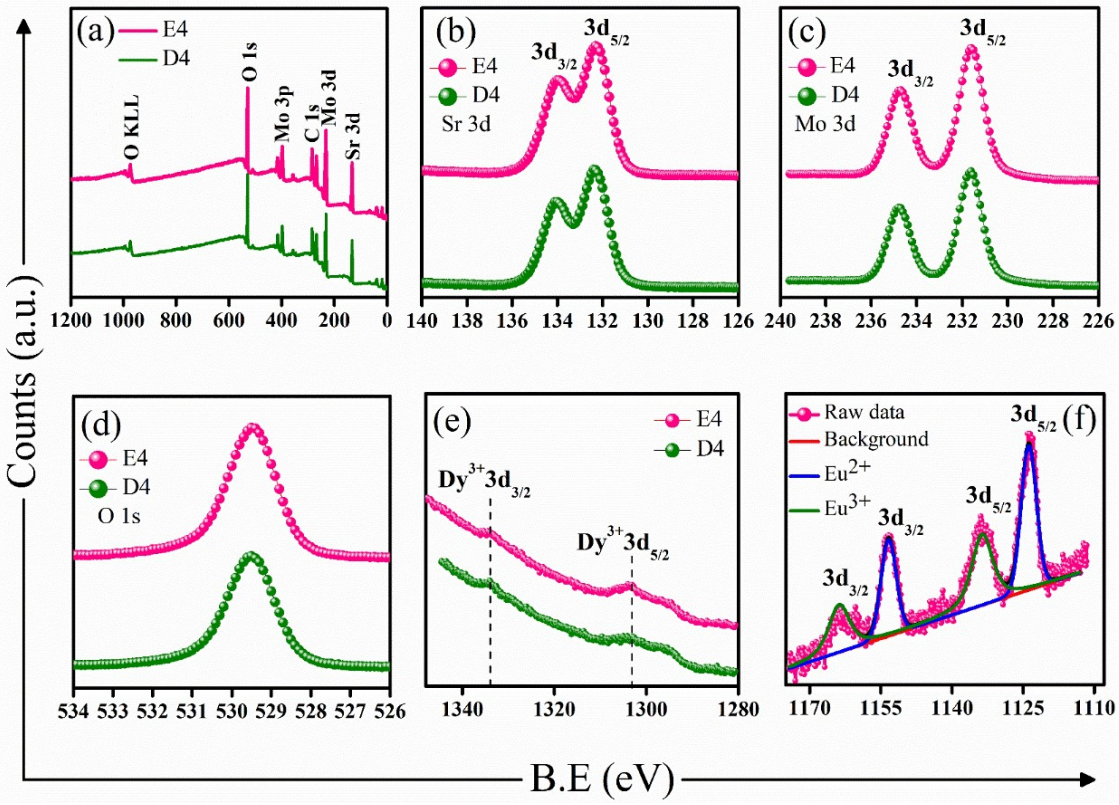

Fig. 5.3 XPS Survey scan **(a)** and XPS graph of **(b)** Sr 3d, **(c)** Mo 3d, **(d)** O 1s, **(e)** Dy 3d spectra for E4 and D4. **(f)** XPS spectrum of Eu 3d for E4 sample.

5.3.2 Absorption and bandgap study

The absorption spectra of the D and E phosphor series are shown in Fig. 5.4 (a). At 264 nm, the CT broadband for D0 is detected, which is because of the charge transfer from O^{2-} → Mo^{6+} ions [20]. The absorption band of Dy^{3+} doped phosphors is slightly moved to the lower energy (higher wavelength) and peaks at 272 nm. The absorption peak further shifts to 317 nm for Eu^{3+} co-doped phosphors. The red-shift in the absorption peak is because of the presence of disorder and defect states due to Dy^{3+} and Eu^{3+} ions [112]. The Dy^{3+} and Eu^{3+} 4f electrons introduce new energy levels close to the conduction band of $SrMoO_4$. Below the conduction band, a new defect band is formed and the transfer of electrons for the O^{2-} to this defect band causes a red shift in the absorption band. A small peak ascribed to the $^7F_0 \rightarrow {}^5D_2$ electronic transition is observed around 464 nm for Eu^{3+} co-doped samples.

The Tauc equation 5.1 is used to compute the bandgap of phosphors [130].

$$\alpha h\nu = A(h\nu - E_g)^n, \tag{5.1}$$

Where α signifies the absorption coefficient, $h\nu$ signifies the energy of photons, and n represents the nature of electronic transitions. The n is taken to be ½ because $SrMoO_4$ exhibits direct allowed electronic transitions [24,113]. Fig. 5.4 (b) depicts the Tauc plot of the prepared phosphors. The E_g is estimated by extending the linear section of the Tauc figure and the x-intercept for $(\alpha h\nu)^2$=0 yields the value of E_g in eV. The calculated value of E_g for D0 is 4.12 eV, and is in accord with our previous work [23]. The value of E_g is lowered as the Dy^{3+} and Eu^{3+} ions are doped in the $SrMoO_4$ matrix. The formation of intermediate defect energy levels of Dy^{3+} and Eu^{3+} ions causes the electrons to flow from O^{2-} to these levels and as a result of which the bandgap is red-shifted.

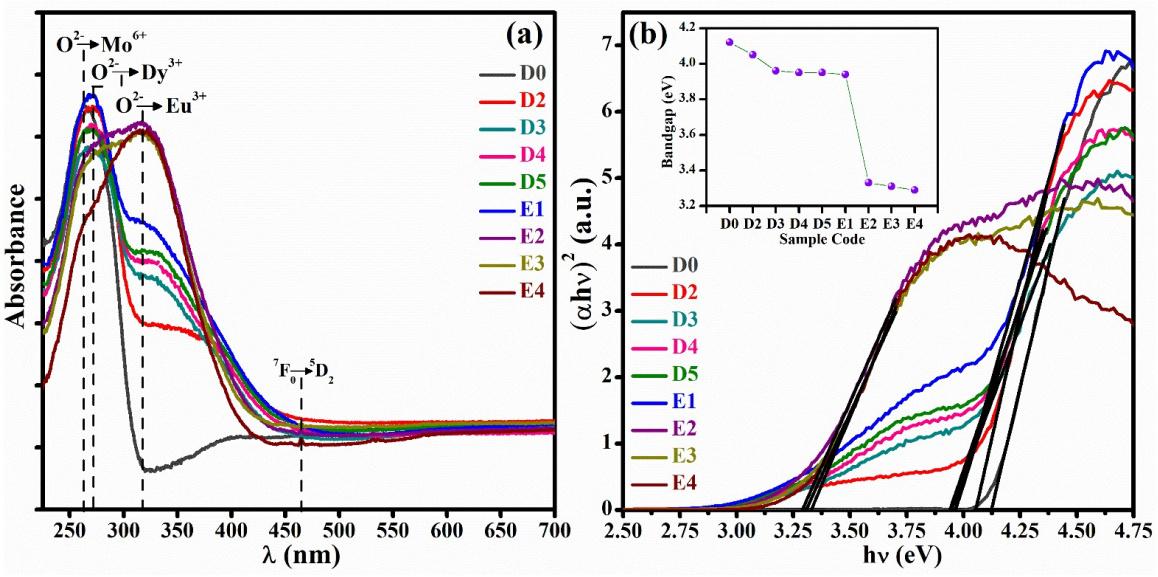

Fig. 5.4 (a) UV-Visible Absorption spectrum of the phosphors. **(b)** Tauc plot of all the phosphors. Inset shows the variation of Bandgap.

5.3.3 PLE and PL analysis

Fig. 5.5 presents the PLE spectrum of D0 examined at 500 nm excitation wavelength. The broadband around 297 nm is the ligand to metal charge transfer (LMCT) band, which is accredited to the charge transfer from $O^{2-} \rightarrow Mo^{6+}$ in $[MoO_4]^{2-}$ groups of $SrMoO_4$ phosphor.

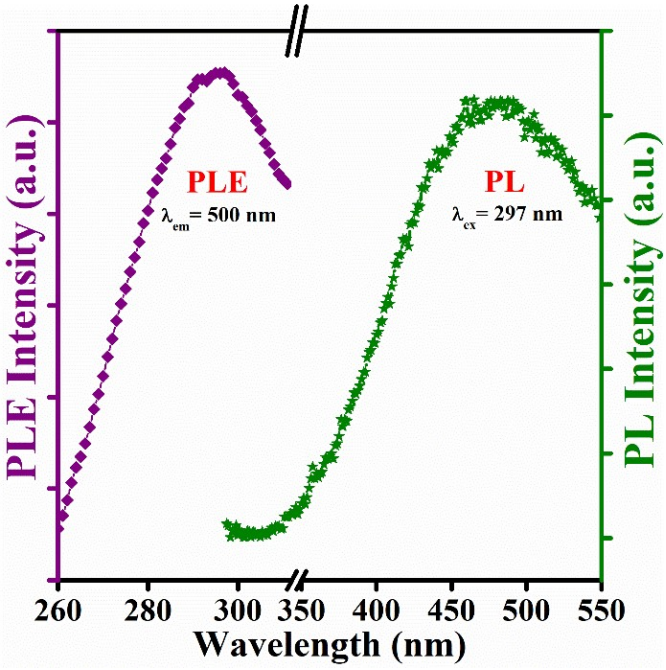

Fig. 5.5 PLE (in violet) and PL (in green) spectrum of D0 phosphor examined at 500 nm emission wavelength and 297 nm excitation wavelength, respectively.

Fig. 5.6 (a) represents the PLE spectrum of Dy^{3+} doped $SrMoO_4$ phosphors examined at 486 nm ($^4F_{9/2}\rightarrow{}^6H_{15/2}$). The broadband is observed because of the overlap between the $O^{2-}\rightarrow Mo^{6+}$ LMCT and $O^{2-}\rightarrow Dy^{3+}$ charge transfer band. The broadband is blue-shifted for Dy^{3+} doped phosphors. Some characteristic peaks corresponding to f-f transitions Dy^{3+} ion 4f configuration are also observed in the PLE spectrum. These peaks are at 327 nm ($^6H_{15/2}\rightarrow{}^6P_{3/2}$), 352 nm ($^6H_{15/2}\rightarrow{}^6P_{7/2}$), 366 nm ($^6H_{15/2}\rightarrow{}^4I_{11/2}$), 388 nm ($^6H_{15/2}\rightarrow{}^4I_{13/2}$), 427 nm ($^6H_{15/2}\rightarrow{}^4G_{11/2}$), and 453 nm ($^6H_{15/2}\rightarrow{}^4I_{15/2}$) [112]. The PLE intensity of the peaks increases with Dy^{3+} concentration and is maximum for D4 phosphor but decreases with further Dy^{3+} doping. The broadband has maximum intensity and is therefore used as excitation wavelength while recording the PL spectrum. Fig. 5.6 (b) presents the PLE spectrum of Eu^{3+} co-doped phosphors examined at 615 nm ($^5D_0\rightarrow{}^7F_2$) emission transition of Eu^{3+} ion.

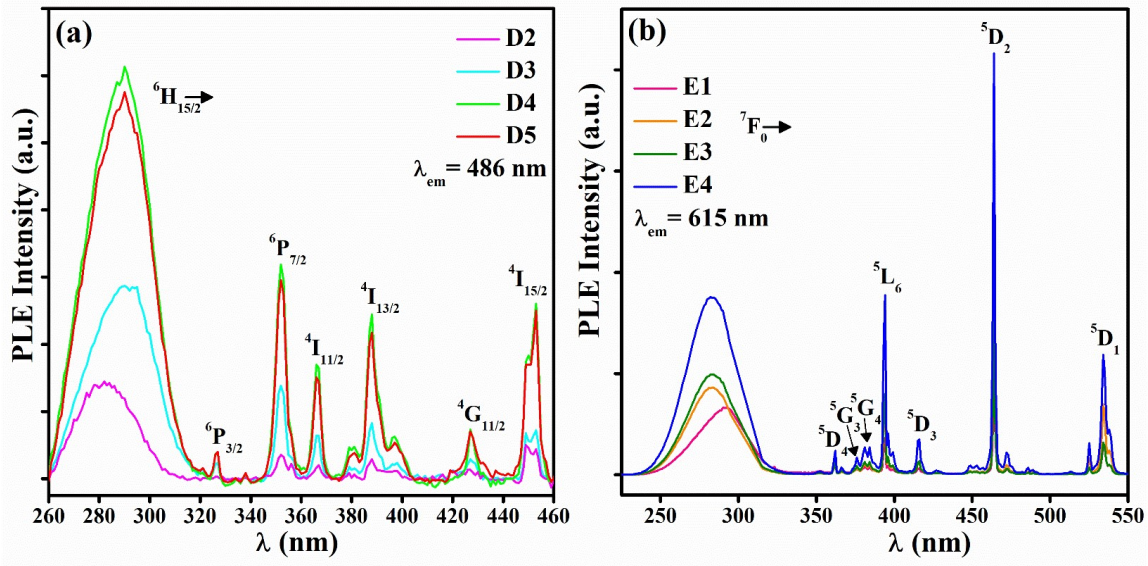

Fig. 5.6 PLE spectrum of **(a)** Dy^{3+} doped phosphors, and **(b)** Eu^{3+} co-doped phosphors.

Similar broadband as in the case of the D series is observed for the E series as well which is accredited to the overlap of $O^{2-}\rightarrow Mo^{6+}$ LMCT and $O^{2-}\rightarrow Dy^{3+}/Eu^{3+}$ charge transfer band. In addition to the broadband, some characteristic intra-configurational 4f electron transition peaks of Eu^{3+} ions are positioned at 362 nm ($^7F_0\rightarrow{}^5D_4$), 376 nm ($^7F_0\rightarrow{}^5G_3$), 384 nm

($^7F_0 \rightarrow {}^5G_4$), 394 nm ($^7F_0 \rightarrow {}^3L_6$), 416 nm ($^7F_0 \rightarrow {}^5D_3$), 464 nm ($^7F_0 \rightarrow {}^5D_2$), and 534 nm ($^7F_0 \rightarrow {}^5D_1$). All the observed excitation peaks in the spectrum are in good agreement with the reported literature [3,112].

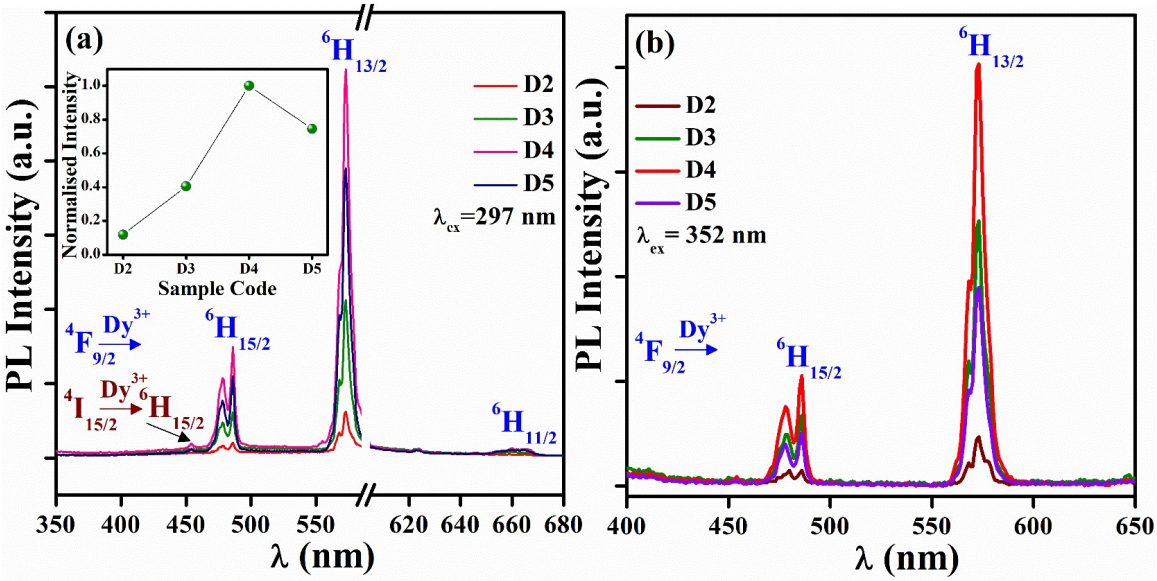

Fig. 5.7 PL spectrum of Dy^{3+} doped phosphors recorded at **(a)** 297 nm and **(b)** 352 nm emission wavelength.

The emission curves of Dy^{3+} doped $SrMoO_4$ phosphors shown in Fig. 5.7 (a) and (b) for 297 nm and 352 nm excitation wavelength reveal a blue (486 nm) emission peak and a strong yellow (573 nm) emission peak corresponding to $^4F_{9/2} \rightarrow {}^6H_{15/2}$ and $^4F_{9/2} \rightarrow {}^6H_{13/2}$ electronic transitions of Dy^{3+} ion [112]. Two weak peaks located at 454 nm and 660 nm corresponding to $^4I_{15/2} \rightarrow {}^6H_{15/2}$ and $^4F_{9/2} \rightarrow {}^6H_{13/2}$ transitions are also observed. All the observed emission peaks corresponding to Dy^{3+} ion are in accord with the previous reports [181]. The hypersensitive electric dipole (ED) transition ($^4F_{9/2} \rightarrow {}^6H_{13/2}$) dominates the spectrum indicating that the Dy^{3+} ions occupy sites of non-inversion symmetry. The $^4F_{9/2} \rightarrow {}^6H_{15/2}$ transition is the magnetic dipole (MD) transition. The inset in Fig. 5.7 (a) depicts the normalized intensity variation of 572 nm peak with varying Dy^{3+} concentration. The intensity of the peak increases with the increasing Dy^{3+} concentration in the host matrix

and attains maximum for the D4 sample. The emission intensity decreases for D5 phosphor because of the concentration quenching.

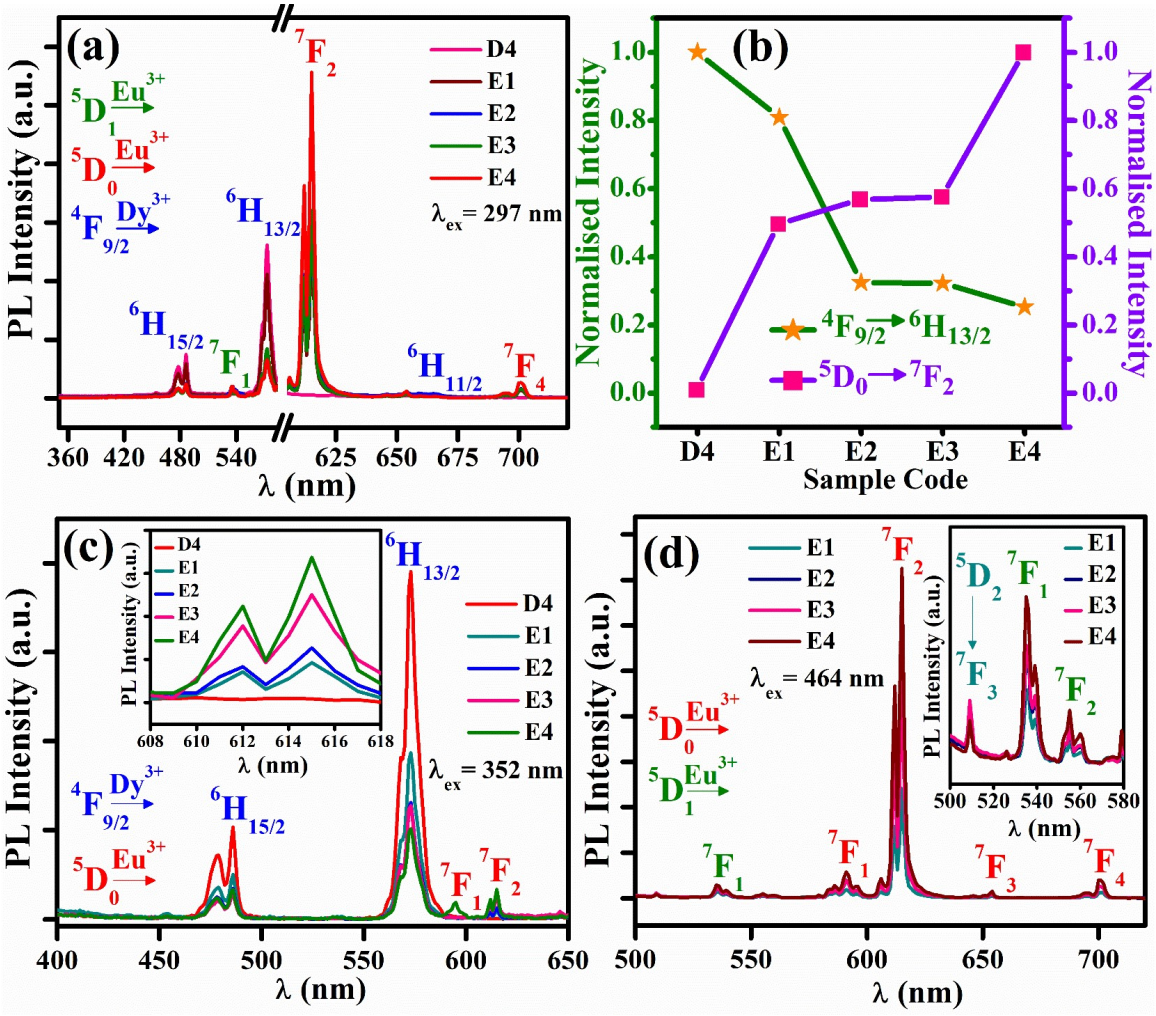

Fig. 5.8 (a) Comparative PL spectra of D4 and E series examined at 297 nm excitation wavelength. **(b)** The normalized intensity variation of $^4F_{9/2}\rightarrow{}^6H_{13/2}$ and $^5D_0\rightarrow{}^7F_2$ peaks as a function of Eu^{3+} doped samples. **(c)** Comparative PL spectra of D4 and E series monitored at 352 nm excitation wavelength. **(d)** Comparative PL spectra of E series monitored at 464 nm excitation wavelength.

Fig. 5.8 (a) presents the comparative PL spectra of D4 and E series phosphors examined at 297 nm excitation wavelength. In addition to the emission peaks corresponding to Dy^{3+} ions, three new emission peaks at 536 nm ($^5D_1\rightarrow{}^7F_1$), 615 nm ($^5D_0\rightarrow{}^7F_2$), and 700 nm ($^5D_0\rightarrow{}^7F_4$), corresponding to Eu^{3+} ion are also observed. However, in the PL analysis we do not observe any broadband attributed to Eu^{2+} ions. The normalized intensity variation

of 573 nm ($^4F_{9/2}\rightarrow{}^6H_{13/2}$) peak and 615 nm ($^5D_0\rightarrow{}^7F_2$) peak with different Eu^{3+} co-doping concentrations is shown in Fig. 5.8 (b). It is noticed that with increasing doping concentration of Eu^{3+} ion, the intensity of 573 nm peak decreases while the intensity of 615 nm peak increases, which suggests that the energy transfer from $[MoO_4]^{2-}$ LMCT band to Eu^{3+} ions is more probable than energy transfer to Dy^{3+} ions. To examine the energy transfer from Dy^{3+} ions to Eu^{3+} ions, the Eu^{3+} doped phosphors were excited with 352 nm wavelength, depicted in Fig. 5.8 (c). The intensity of the emission peaks corresponding to the electronic transitions in the Eu^{3+} ions is very weak as compared to the Dy^{3+} ion emission peaks, which clarifies that the energy transfer from Dy^{3+} to Eu^{3+} ions is poor. Fig. 5.8 (d) depicts the PL spectrum of the E series phosphors examined at 464 nm excitation wavelength. Some of the characteristic emission peaks of Eu^{3+} ions are observed at 509 nm ($^5D_2\rightarrow{}^7F_3$), 535 ($^5D_1\rightarrow{}^7F_1$), 555 nm ($^5D_1\rightarrow{}^7F_2$), 591 nm ($^5D_0\rightarrow{}^7F_1$), 615 nm ($^5D_0\rightarrow{}^7F_2$), 654 nm ($^5D_0\rightarrow{}^7F_3$), and 700 nm ($^5D_0\rightarrow{}^7F_4$) [182,183]. The $^5D_0\rightarrow{}^7F_1$ transition of Eu^{3+} at 591 nm is allowed by MD transition and is unaffected by Eu^{3+} ion surrounding, whereas the $^5D_0\rightarrow{}^7F_2$ transition of Eu^{3+} at 615 nm is allowed by ED transition and is hypersensitive to the local symmetry of the Eu^{3+} ion [183]. The fact that the ED transition is much more intense than the MD transition indicates that Eu^{3+} at the Sr^{2+} site deviates from its inversion symmetry and the local symmetry around the Eu^{3+} ion is low [183]. Moreover, when Eu^{3+} is doped in $SrMoO_4$, there is a charge and size mismatch which causes cation vacancies and lattice strain, respectively. These cause a distorted local environment around Eu^{3+} ions and a lowering of symmetry, which causes an intense ED transition peak. The splitting in the emission peaks is called the stark splitting and it is due to the ligand field effect when rare-earth ions are inserted into a ligand environment.

5.3.4 Energy transfer dynamics

The non-radiative energy transfer among the RE ions at higher doping concentrations results in the concentration quenching of emission peaks. A non-radiative energy transfer can occur by one of three mechanisms: exchange interaction, radiative reabsorption, or electric multipolar interaction. The radiative reabsorption requires a substantial overlap between the emission and the excitation spectra. As a consequence of the limited spectrum overlap between the Dy^{3+} emission and Eu^{3+} excitation, radiation reabsorption is neglected in this scenario. The donor and acceptor wave functions must have a considerable direct or indirect overlap for exchange interactions to take place. According to the Van Uitert theory, the critical separation distance (R_c) between the emitting ions for wavefunction overlapping must be less than 5 Å [184]. The R_c in the case of Dy^{3+}/Eu^{3+} co-doped $SrMoO_4$ is evaluated using the formula derived by Blasse [136],

$$R_c = 2\left(\frac{3V}{4\pi x_c N}\right)^{\frac{1}{3}} \tag{5.2}$$

Where the volume of $SrMoO_4$ is designated by V and from XRD analysis, it is calculated to be 347.53 $Å^3$. The value of x_c represents the total critical concentration of Dy^{3+} and Eu^{3+} ions which is 0.08. The number of Dy^{3+} occupied sites is represented by N, which is 4 for the $SrMoO_4$ lattice. The evaluated critical distance of $SrMoO_4$:Dy^{3+}, Eu^{3+} phosphor is 12.75 Å, which is substantially more than the critical distance constraint. This rules out the possibility of an exchange interaction process for non-radiative energy transfer. Therefore, the non-radiative energy transfer could be only due to the electric multipolar interaction. Electric multipolar interactions are classified as dipole-dipole, dipole-quadrupole, and quadrupole-quadrupole. The type of multipolar interaction can be asserted by Dexter's energy transfer mechanism for multipolar interaction and Reisfeld's approximation [185],

$$\left(\frac{I_0}{I}\right) \propto C^{n/3} \tag{5.3}$$

Where I and I_0 denote the PL intensity of Dy^{3+} in the presence and absence of Eu^{3+}, respectively. The total doping concentration of the Dy^{3+} and Eu^{3+} ions is represented by C. $I_0/I \propto C^{n/3}$, with n = 6, 8, and 10 related to dipole-dipole, dipole–quadrupole, and quadrupole–quadrupole interactions, respectively. The plots of I_0/I as a function of $C^{n/3}$ are presented in Fig. 5.9 (a). The linear dependency of the dipole-dipole interaction is the best fitting solution as presented in Fig. 5.9 (a). This suggests that the transfer of energy from Dy^{3+} to Eu^{3+} is primarily a dipole-dipole interaction.

Fig. 5.9 (b) depicts the schematic of the energy transfer process utilized to inspect the mechanism of energy transfer in $SrMoO_4$:Dy^{3+}, Eu^{3+} phosphors. The emission broadband of the $SrMoO_4$ host peaks around 500 nm (in Fig. 5.5) and it overlaps with the excitation spectra of Dy^{3+} and Eu^{3+} ions (in Fig. 6), implying the possibility of the energy transfer from the $[MoO_4]^{2-}$ LMCT band to Dy^{3+} and Eu^{3+} ions. When the electrons in the 2p valance band of the O^{2-} absorb 297 nm UV photons, they are excited to the Mo^{6+} 4d conduction band. After that, electrons fall to the lower energy levels of Dy^{3+} ions and Eu^{3+} ions emitting yellow and red emissions, respectively. It should be noted that when the co-doping concentration of the Eu^{3+} ion is increased, the intensity of the Eu^{3+} emission increases while the intensity of the Dy^{3+} emission decreases (in Fig. 5.8 (a)). For the E4 sample, the intensity of the peak at 615 nm ($^5D_0 \rightarrow {}^7F_2$) is more than the peak at 573 nm ($^4F_{9/2} \rightarrow {}^6H_{13/2}$). The reason behind this could be that the intense excitation peak of the Eu^{3+} ion at 464 nm lies much closer to the broadband emission peak of the $[MoO_4]^{2-}$ LMCT band, which prompts effective energy transfer from $[MoO_4]^{2-}$ LMCT band to Eu^{3+} levels. To study the energy transfer process from Dy^{3+} to Eu^{3+} ion, we have recorded the PL spectra of co-doped

samples excited by 352 nm. The intensity of the Eu^{3+} emission peaks is very less in comparison to the Dy^{3+} emission peaks, indicating the weak energy transfer from Dy^{3+} to Eu^{3+}. The energy transfer from $[MoO_4]^{2-}$ LMCT band to Dy^{3+} and Eu^{3+} energy levels are marked with ET1 and ET2, respectively, and the energy transfer from Dy^{3+} to Eu^{3+} ions is marked with ET3 in the energy diagram schematic presented in Fig. 5.9 (b).

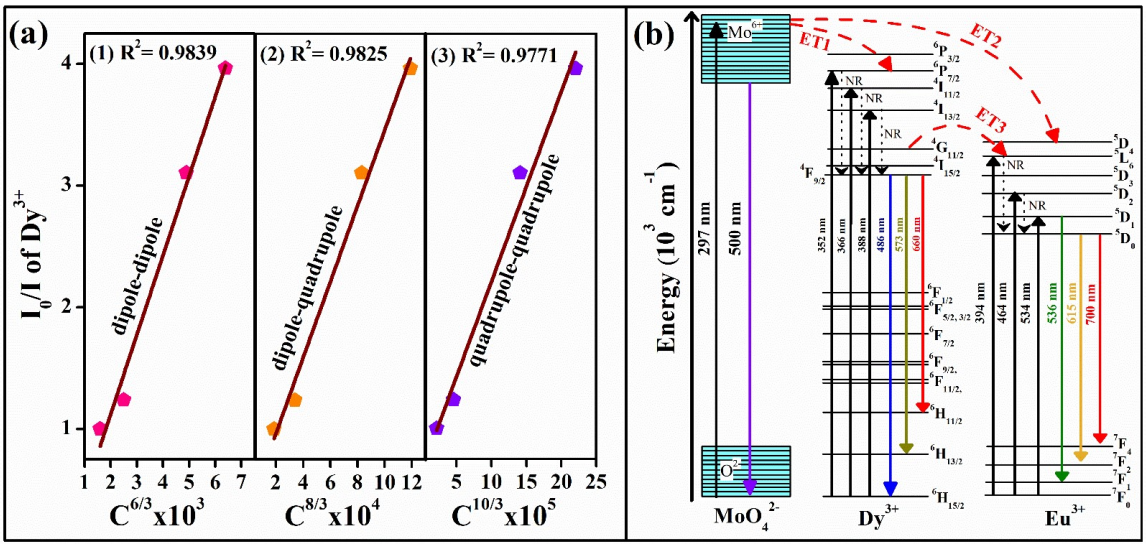

Fig. 5.9 (a) I_0/I as a function of **(1)** $C^{6/3}$, **(2)** $C^{8/3}$, and **(3)** $C^{10/3}$ **(b)** Schematic of the energy transfer phenomenon in $SrMoO_4:Dy^{3+}$, Eu^{3+}.

5.3.5 PL Decay study

Fig. 5.10 (a) and (b) present the decay graphs of D4 and E4 phosphors monitored at 352 nm excitation ($^6H_{15/2} \rightarrow {}^6P_{7/2}$) and 573 nm emission ($^4F_{9/2} \rightarrow {}^6H_{13/2}$), respectively. The bi-exponential function in equation (5.4) is used to fit the decay curves [150],

$$I(t) = I_0 + B_1\, exp\left(-\frac{t}{\tau_1}\right) + B_2\, exp\left(-\frac{t}{\tau_2}\right) \qquad (5.4)$$

Where τ_1 signifies fast decay time and τ_2 signifies slow decay time of the $^4F_{9/2}$ level of the Dy^{3+} ion; I_0 is the background intensity after prolonged excitation; B_1 and B_2 are constants. The average lifetime is evaluated using the following equation [23]:

$$\tau_o = (A_1\tau_1^2 + A_2\tau_2^2)/(A_1\tau_1 + A_2\tau_2) \quad (5.5)$$

According to the equation 5.5, the average lifetime of the $^4F_{9/2}$ level of the Dy^{3+} for D4 and E4 is 0.936 ms and 0.894 ms, respectively. After Eu^{3+} co-doping, the lifetime of Dy^{3+} ions is reduced, validating the energy transfer mechanism from Dy^{3+} to Eu^{3+} ions.

The equation 5.6 is utilized for the computation of energy transfer efficiency (η_{ET}),

$$\eta_{ET} = 1 - \frac{\tau_x}{\tau_o} \quad (5.6)$$

Where τ_o and τ_x are the average lifetime of the $^4F_{9/2}$ level. The calculated value of η_{ET} is 4.69%, indicating weak energy transfer from Dy^{3+} to Eu^{3+} ions in $SrMoO_4$.

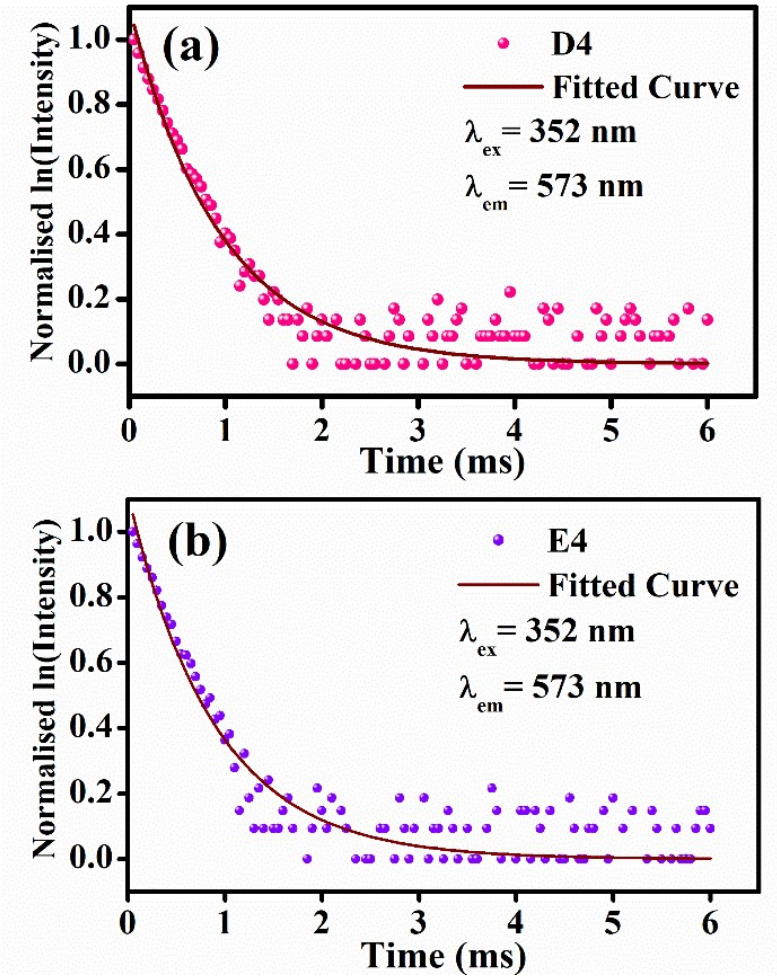

Fig. 5.10 PL decay curve of **(a)** D4 and **(b)** E4 phosphors.

5.3.6 Tunable color study of Dy^{3+}/Eu^{3+} co-doped $SrMoO_4$

Fig. 5.11 presents the Commission Intentional de I'eclairage (CIE) diagram of the prepared phosphors as determined by their respective PL spectra and the CIE coordinates along with color correlated temperature (CCT) and color purity tabulated in Table 5.3. Fig. 5.11 (a) depicts the CIE diagram of the Dy^{3+} doped and Dy^{3+}/Eu^{3+} co-doped phosphors when excited by 297 nm wavelength. With an increase in Dy^{3+} concentration, the overall emission shifts towards the yellow region but after Eu^{3+} co-doping, the emission shifts towards the red region. Fig. 5.11 (b) depicts the CIE diagram of Dy^{3+} doped phosphors when excited by 352 nm wavelength. It is observed that the overall emission of D2 phosphor lies in the neutral white region with color purity and the emission of D4 phosphor is shifted more towards the yellow region with color purity. Therefore, the variation in the overall color of Dy^{3+} doped phosphors is more when excited by 352 nm. Fig. 5.11 (c) depicts the CIE diagram for the E4 sample, excited with different wavelengths. It is observed that the overall emission of the E4 phosphor can be adjusted from warm white to red color by altering the excitation wavelength. As a result, by altering concentration and excitation wavelength, the color of the Dy^{3+}/Eu^{3+} doped $SrMoO_4$ phosphors can be tuned.

The CCT of the prepared phosphors is calculated using McCAMY's approximated equation [151].

$$CCT = 5520.33 - 6823n + 3525n^2 - 449n^3 \quad (5.7)$$

Where x_e and y_e are the chromaticity epicenters (0.338, 0.186), x and y represent the CIE coordinates, and the inverse slope line is represented by $n = \frac{(x-x_e)}{(y-y_e)}$.

The following expression is used to evaluate the color purity (CP) which is the measure of monochromaticity,

$$color\ purity\ (\%) = \frac{\sqrt{(x_s - x_i)^2 + (y_s - y_i)^2}}{\sqrt{(x_d - x_i)^2 + (y_d - y_i)^2}} \quad (5.8)$$

Where (x_s, y_s) are the sample emission color coordinates relative to the standard CIE1931 coordinates $(x_i = 0.3333, y_i = 0.3333)$ and (x_d, y_d) are the dominant wavelength coordinates. The dominant wavelength coordinates are derived by drawing a straight line from the (x_i, y_i) and (x_s, y_s) points to cut the point on the perimeter of the CIE color space.

Table 5.3 CIE coordinates, CCT value, and CP of prepared phosphors.

Sample Code	Excitation Wavelength	(x, y)	CCT (K)	CP (%)
D2	297	(0.3874, 0.3983)	4072	35.8
	352	(0.3408, 0.3395)	5135	4.1
D3	297	(0.3812, 0.4201)	4363	40.5
	352	(0.3695, 0.4043)	4461	32.3
D4	297	(0.3939, 0.4409)	4195	50.6
	352	(0.4055, 0.4642)	3975	61.1
E1	297	(0.4612, 0.4168)	2826	63.6
E2	297	(0.3121, 0.3945)	2072	13.3
E3	297	(0.3205, 0.3952)	2002	15.3
E4	297	(0.5589, 0.3750)	1590	80.3
	352	(0.4054, 0.4053)	3612	43.3
	464	(0.6302, 0.3663)	1174	99.1

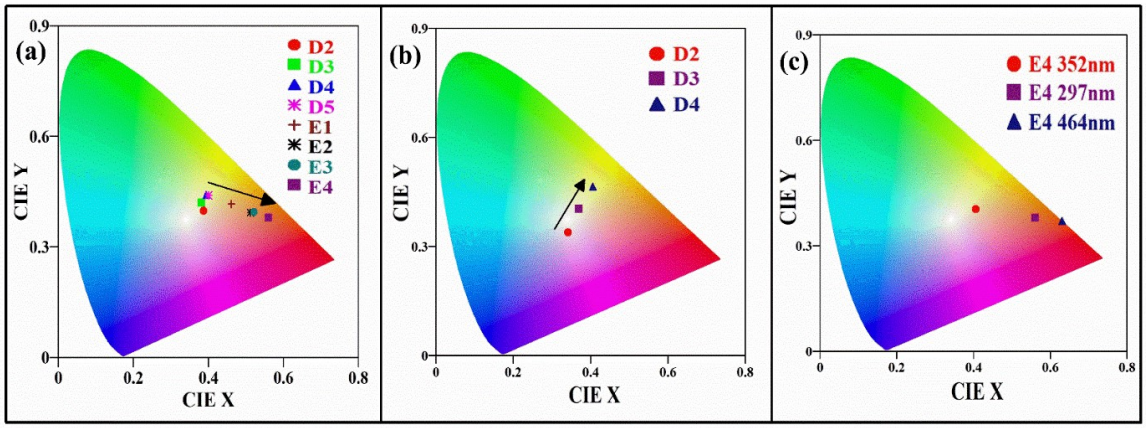

Fig. 5.11 CIE chromaticity diagram of **(a)** Dy^{3+}/Eu^{3+} co-doped $SrMoO_4$ phosphors under 297 nm excitation, **(b)** Dy^{3+} doped $SrMoO_4$ phosphors examined at 352 nm excitation, and **(c)** E4 phosphor under different excitation wavelengths.

5.3.7 Fluorescence Thermometry

The dependence of emission intensity on the temperature corresponding to the Dy^{3+} and Eu^{3+} ions can be utilized for the fluorescence thermometry application. Fig. 5.12 (a) and (b) presents the temperature-dependent PL spectra of D4 phosphor examined at 297 nm and 352 nm excitation wavelength, respectively, for the 300 K – 520 K temperature range. It is observed that when excited with 297 nm wavelength, all emission peaks of Dy^{3+} ions show an increasing trend with temperature. This increase in PL intensity of all the peaks is because of the anti-thermal quenching phenomenon. However, when excited with 352 nm, the peaks originating from the $^4F_{9/2}$ energy level of Dy^{3+} ion decrease while the intensity of the peak corresponding to $^4I_{15/2} \rightarrow {}^6H_{15/2}$ (at 454 nm) increases. This contrasting PL intensity variation in D4 phosphor with temperature is because of the thermally coupled nature of $^4I_{15/2}$ and $^4F_{9/2}$ energy levels of Dy^{3+} ion [46]. As the temperature increases, the relative population of the thermally coupled levels is governed by the Boltzmann distribution law and electrons tend to go from $^4F_{9/2}$ to $^4I_{15/2}$ energy level because of which the PL intensity of 454 nm peak increases while that of others decreases [46]. Fig. 5.12 (c) and (d) depict the temperature-dependent PL spectra of E4 phosphor examined at 464 nm and 297 nm,

respectively, for the 300 K – 520 K temperature range. The PL intensity corresponding to the Eu^{3+} ion gradually decreases in both cases. The inset in Fig. 5.12 (d) depicts the normalized intensity variation of 572 nm ($^4F_{9/2}\rightarrow{}^6H_{13/2}$) and 615 nm ($^5D_0\rightarrow{}^7F_2$) peaks of Dy^{3+} and Eu^{3+} ions with temperature, respectively.

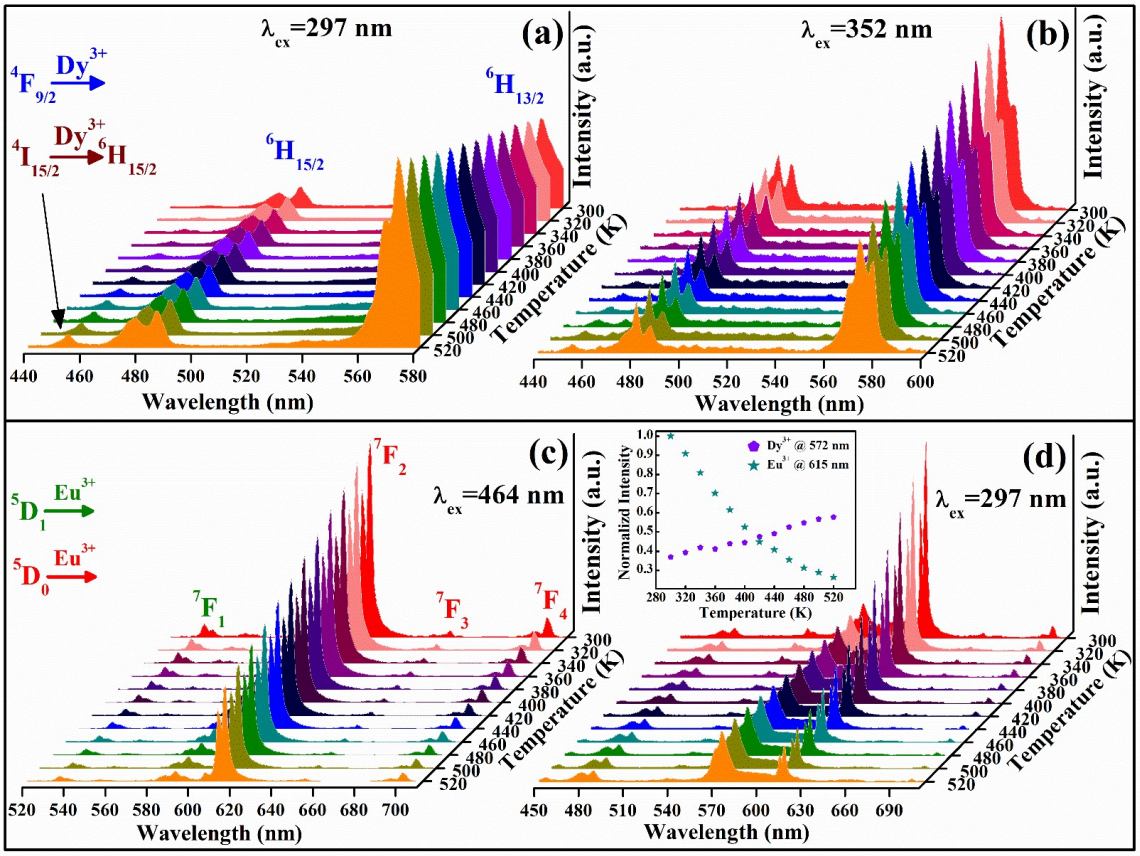

Fig. 5.12 Temperature-dependent PL of D4 phosphor examined at **(a)** 297 nm, **(b)** 352 nm. Temperature-dependent PL of E4 phosphor examined at **(a)** 464 nm, **(b)** 297 nm. Inset shows the variation of 372 nm and 615 nm peaks in E4 phosphor with temperature.

The contrasting response of Dy^{3+} and Eu^{3+} emission to temperature can be utilized for FIR-based fluorescence thermometry. The FIR (I_{Dy}/I_{Eu}) is given by the equation 5.9 [186],

$$FIR = \frac{I_{572}}{I_{615}} = A + Bexp(-\Delta E/kT) \tag{5.9}$$

Where ΔE is the necessary activation energy for the nonradiative process, k represents the Boltzmann constant, A represents the proportional parameter, and B represents an offset

parameter. The FIR variation with temperature is presented in Fig. 5.13 (a). Fig. 5.13 (b) depicts the ln (FIR) vs. 1/T plot, where the slope of the linearly fitted line reveals the value of activation energy that is 1315.632 cm^{-1}. The thermal sensitivity can further be investigated by evaluating the absolute and relative sensitivity by the equations 5.10 and 5.11 [186],

$$S_a = \left|\frac{\partial FIR}{\partial T}\right| = Cexp(-\Delta E/kT) \times \frac{\Delta E}{kT^2} \tag{5.10}$$

$$S_r = \left|\frac{1}{FIR}\frac{\partial FIR}{\partial T}\right| \times 100\% \tag{5.11}$$

Where the relative sensitivity (S_r) is independent of the operational principle of thermometry and represents the relative change of the FIR per degree of temperature change (in % K^{-1}), i.e. FIR ratio. The dependence of S_a and S_r on temperature is depicted in Fig. 5.13 (c) and (d), respectively. The enhancement in S_a is seen with temperature with the maximum S_a (1.06×10^{-2} K^{-1}) at 520 K. The S_r value is considered the critical parameter for the practical application. The maximum S_r value (1.46 % K^{-1}) is obtained at 300 K and decreases with increasing temperature. The S_r value at various temperatures and its comparison with some of the data reported in other literature is tabulated in Table 5.4. The high S_r value indicates good signal sensing capability of the phosphor. The CIE coordinates of the E4 sample at 300 K, 420 K, and 520 K are presented in the CIE diagram depicted in Fig. 5.14 (b). The well-separated peaks of Dy^{3+} (572 nm) and Eu^{3+} (615 nm) result in the good color discriminability of the E4 phosphor with increasing temperature, which is vital for temperature detection.

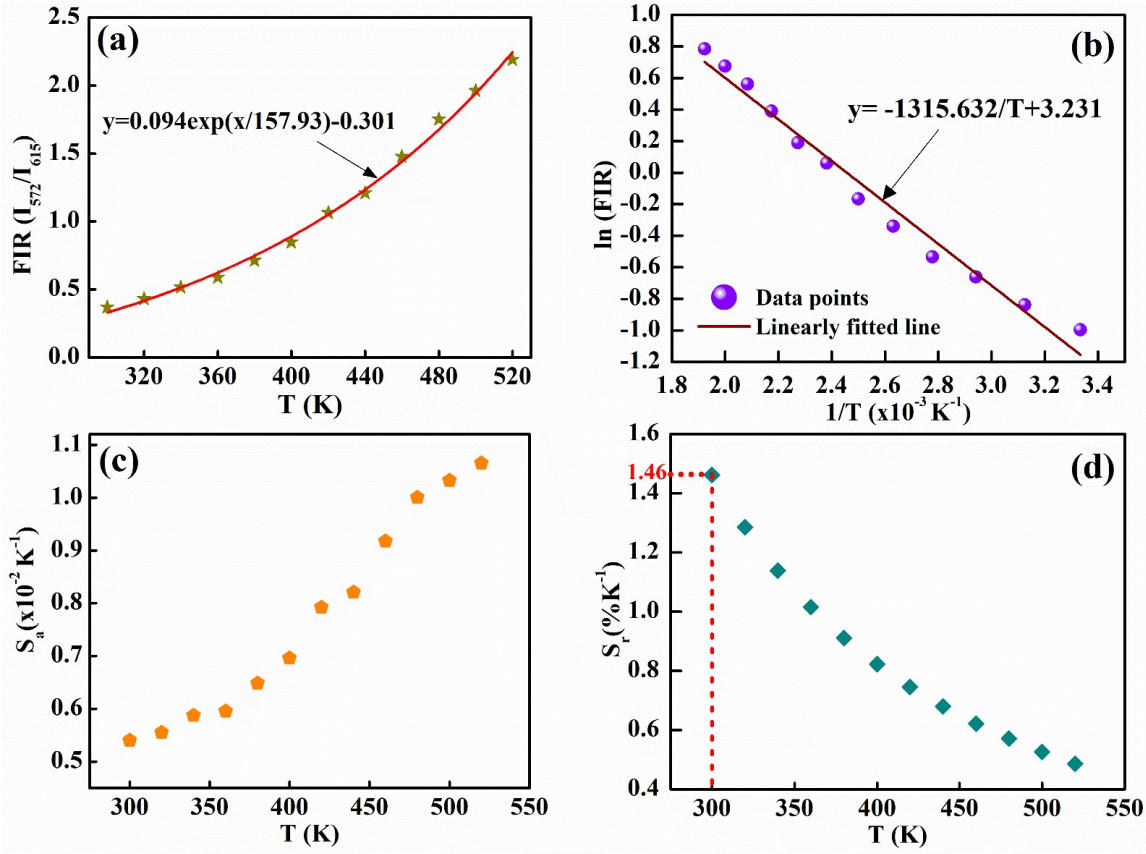

Fig. 5.13 (a) The FIR variation with temperature, **(b)** plot of ln (FIR) vs. 1/T, **(c)** absolute sensitivity (S_a), and **(d)** relative sensitivity (S_r) as a function of temperature for E4 phosphor.

The configurational coordinate diagram (CCD), shown in Fig. 5.14 (a), helps explain the process underlying the contrasted variance in PL intensity related to the Dy^{3+} and Eu^{3+} ions. The CCD depicts Born-Oppenheimer potential energy parabolic U_g and U_e curves representing the ground and excited states of the system, respectively, as a function of generalized configurational coordinate 'Q'. The U_e state is formed as a result of $O^{2-} \rightarrow Mo^{6+}$ LMCT and $O^{2-} \rightarrow Dy^{3+}$ CTB. The yellow and red parabola represents the electronic states of Dy^{3+} and Eu^{3+} ions, respectively. At room temperature (300 K), the electrons after absorbing photons will be excited from the U_g to U_e state (path 1). After absorption, the electrons reach the bottom of the U_e state by vibrational relaxation (path 2). Then the electrons can transfer to the $^4F_{9/2}$ level of Dy^{3+} (path 3) or $^5D_0$ level of Eu^{3+} ion (path 4).

The electrons then revert to the corresponding ground states emitting characteristic emission lines of Dy^{3+} and Eu^{3+} ions. With temperature rise, the lattice vibrations become stronger and the thermally active phonons increase. The electrons near the bottom of the U_e band pair with the thermally active phonons, and their energies approach the crossover point A. These electrons move to the $^4F_{9/2}$ energy level of the Dy^{3+} ion (path 5). Therefore, as the temperature rises, the no of electrons in the $^4F_{9/2}$ energy level of the Dy^{3+} ion increases (by paths 3 and 5), which increases the PL intensity of the Dy^{3+} ion. The electron-phonon interaction becomes stronger as temperature rises and more and more electrons follow path 5, therefore, there is a shortage of electrons following path 4 which results in the decrease in the PL intensity of Eu^{3+} ions. This explains the nature of temperature-dependent PL of Dy^{3+}/Eu^{3+} co-doped $SrMoO_4$.

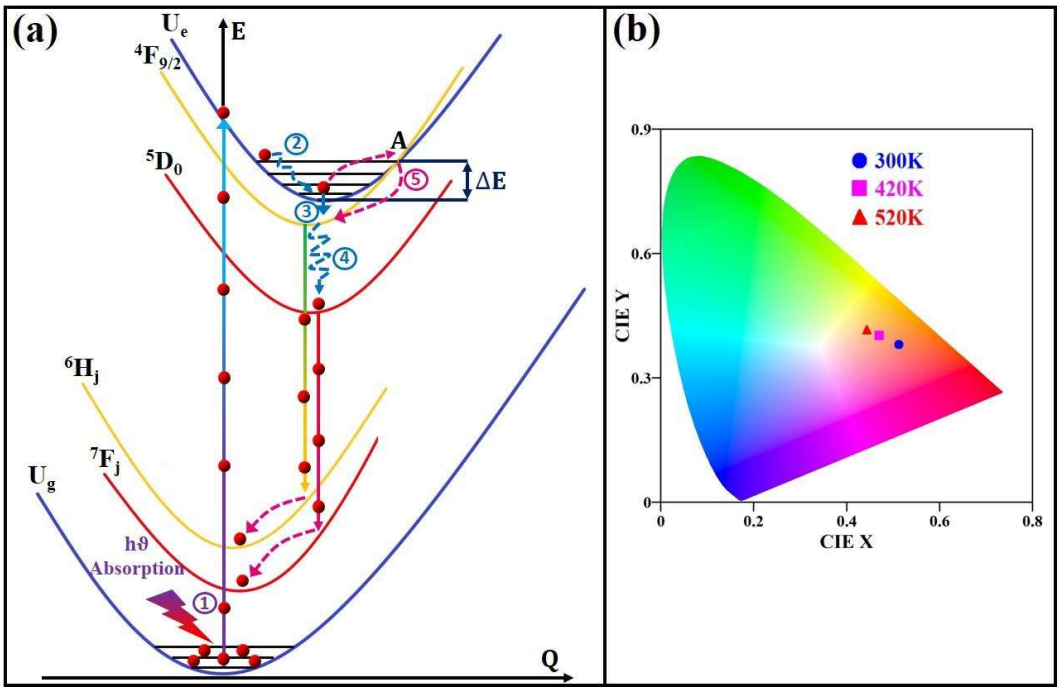

Fig. 5.14 (a) Configurational coordinate diagram for explaining the temperature-induced fluorescence processes in E4 phosphor. **(b)** CIE color coordinates of E4 sample examined at 297 nm excitation wavelength and different temperatures presented in CIE diagram.

Table 5.4 Comparison of relative sensitivity for reported phosphors and synthesized E4 phosphor.

Host	Activated ions	S_r (% K^{-1})	T (K)	Reference
$KBaGd(WO_4)_3$	Dy^{3+}/Eu^{3+}	0.64	458	[164]
$MgAl_2O_4$	Dy^{3+}/Eu^{3+}	0.24	420	[180]
$BaLa_4Si_3O_{13}$	Dy^{3+}/Eu^{3+}	1.46	497	[186]
$GdVO_4$	Dy^{3+}/Eu^{3+}	0.016	298	[187]
LaOBr	Ce^{3+}/Tb^{3+}	0.42	433	[188]
$Mg_3Y_2Ge_3O_{12}$	Eu^{3+}/Mn^{4+}	0.019	300	[189]
$SrMoO_4$	Dy^{3+}/Eu^{3+}	1.46 0.74 0.48	300 420 520	This work

4.4 Conclusion

In conclusion, a facile urea-assisted auto-combustion method was used to prepare Dy^{3+}/Eu^{3+} co-doped $SrMoO_4$ phosphors. The structural analysis validates the formation of the tetragonal crystal structure of the phosphors. The absorbance spectra ascertain the shift in the absorbance peak after Dy^{3+} and Eu^{3+} doping, which is attributed to the energy levels generated within the bandgap of $SrMoO_4$. The PL emission of Dy^{3+}/Eu^{3+} co-doped samples was monitored at different excitation wavelengths. For the co-doped samples, the PL intensity of Eu^{3+} ions is greater for 297 nm excitation than for 352 nm excitation. This is because of the effective transfer of energy from $[MoO_4]^{2-}$ LMCT band to Eu^{3+} energy levels and inefficient transfer of energy from Dy^{3+} to Eu^{3+} ions. The reduction in the lifetime of the $^4F_{9/2}$ level of Dy^{3+} with Eu^{3+} co-doping confirms the weak energy transfer from Dy^{3+} to Eu^{3+} ions. Dexter's energy transfer theory indicates that the energy transfer from Dy^{3+} to Eu^{3+} follows a non-radiative dipole-dipole interaction. The emitting color of the co-doped samples can be adjusted from white to greenish-yellow and greenish-yellow to reddish-

orange by precisely controlling the contents of Dy^{3+} and Eu^{3+} ions and by modulation of excitation wavelength. The synthesized Dy^{3+} doped $SrMoO_4$ phosphors exhibit an anti-thermal phenomenon owing to the energy transfer from the conduction band of $[MoO_4]^{2-}$ to the Dy^{3+} energy levels. The contrasting nature of Dy^{3+} and Eu^{3+} PL emission with temperature is used to probe the temperature sensing property of the Dy^{3+}/Eu^{3+} co-doped $SrMoO_4$ phosphor. Based on FIR mode, the S_r value for 4% Eu^{3+} co-doped $SrMoO_4$:4Dy^{3+} phosphor is 1.46% K^{-1} at 300 K. The configurational coordinate diagram is used to demonstrate the nature of temperature-dependent PL of Dy^{3+}/Eu^{3+} co-doped $SrMoO_4$ phosphor.